Molecular dynamics study of mechanical deformation in cesium lead halide perovskites

Amith Adoor Cheenady and Krishna Rajan[*]

Department of Materials Design and Innovation, University at Buffalo, Buffalo, New York 14260-1660, USA

Mechanical response of single-crystal $CsPbI_3$, $CsPbBr_3$, $CsPbIBr_2$, and $CsPbI_2Br$ is investigated under uniaxial tension and compression using molecular dynamics (MD) simulations. Stress-strain curves for these metal-halide perovskites are determined and mechanisms that strengthen and weaken them under plastic deformation are revealed. Our study finds the mechanical response of these crystals to differ considerably under uniaxial tension and compression. While $CsPbI_3$ and $CsPbBr_3$ exhibit a smooth elastic to plastic transition under uniaxial tension, distinct elastic and plastic regimes are observed under uniaxial compression. Only $CsPbI_3$ is noted to exhibit strain hardening under uniaxial compression, which is deciphered to arise from generation of defects in the plastic regime. These defects, which take the form of deformation-induced distortion of the Pb-I octahedra, are shown to manifest as superlattice reflections in optical diffraction patterns derived from fast Fourier transform analysis of MD simulations. While a perfectly plastic postyield response is observed in $CsPbIBr_2$ and $CsPbI_2Br$ under tension, a monotonic reduction in stress occurs after yielding under compression. Formation and growth of bands of high von Mises shear strain is revealed as an important plastic deformation mechanism in $CsPbIBr_2$ and $CsPbI_2Br$ under uniaxial tension and compression. The evolution of defect microstructure with strain discussed here is expected to provide insights into plausible mechanisms that operate in metal-halide perovskites under experiments such as nanoindentation, while the defect-induced strengthening demonstrated here points to the possibility of fabricating robust perovskite films by engineering defects into the material.

I. INTRODUCTION

Metal-halide perovskites (MHPs) offer wide potential applications as photovoltaics [1], field-effect transistors [2], light-emitting diodes [3], lasers [4], and photodetectors [5] due to their ease of fabrication [6], favorable light-absorption coefficients [2], high charge-carrier diffusion lengths [7], tunable band gaps [8], and multicolor emission [9]. Thus, understanding the elastic response, plastic response, and fracture behavior of MHPs is important for realizing their diverse applications. Given their brittle nature, fracture is accompanied by negligible plasticity in MHPs under flexure [10], uniaxial tension [11], and uniaxial compression [12]. Kim *et al.* [10] observed mode-I fracture in $CsPbBr_3$ and $MAPbI_3$ (MA = methylammonium) thin films subjected to microbending tests and demonstrated that introduction of residual compressive strains into the films improved their fracture resistance [10]. Fracture driven by intergranular crack propagation was also noted in uniaxial microtensile tests of $MAPbBr_3$ by Lee *et al.* [11]. The performance of perovskite solar cells (PSCs) under mechanical loading, quantified through power-conversion efficiency (PCE), has also been of interest. Park *et al.* [13] noted a marginal drop in PCE when a PSC comprising chlorine-doped $MAPbI_3$ was subjected to 1000 bending cycles at a radius of curvature of 1 mm, while the reduction in PCE was substantial (from 10.75 to 6.1%) when subjected to severe random crumpling [13]. Despite the brittle nature of MHPs, they exhibit extensive plastic deformation in nanoindentation experiments [12–14] due to suppression of fracture by the imposed triaxial state of compressive stress. For instance, the stress-strain curve for chlorine-doped $MAPbI_3$ obtained by Park *et al.* [13] through nanoindentation exhibited strain hardening. Strain hardening also explained the slowdown in the rate of penetration under nanoindentation in single-crystal $MAPbI_3$, $MAPbBr_3$, and $CsPbI_3$ observed by Martinez *et al.* [14]. Furthermore, scanning electron micrographs of single-crystal $MAPbI_3$ and $MAPbBr_3$ subjected to nanoindentation reveal slip bands [14], while dislocation glide and climb have been invoked to explain the high-stress exponents observed in these crystals during nanoindentation creep experiments [12].

Despite the successes of experimental techniques in elucidating the mechanical response of MHPs, they have certain shortcomings. It is difficult to process MHPs to sizes required for established macroscopic standard tests [1]. Further, since brittle fracture governs failure of MHPs under uniaxial tension [11] and compression [12], a triaxial state of stress (as occurring in nanoindentation studies) is required to experimentally investigate the plastic response of MHPs. While such nanoindentation experiments have indeed shed light on mechanisms underlying strain hardening and plastic deformation in MHPs (e.g., dislocation slip [14,15]), a detailed analysis of the evolution of defect microstructure as the material is mechanically loaded lies outside the scope of such techniques. Thus, computational methods such as classical molecular dynamics (MD) simulations, through their high spatiotemporal

[*]krajan3@buffalo.edu

resolution, can complement experiments in deepening our understanding of deformation mechanisms in MHPs at the atomistic scale. Yu *et al.* [16], investigated the mechanical response of single-crystal and polycrystalline MAPbI$_3$ to uniaxial tension using MD simulations. While single-crystal MAPbI$_3$ exhibited higher ultimate strength than the polycrystalline samples, the latter exhibited substantially higher ductility and fracture toughness [16]. The polycrystalline samples also exhibited a reduction in yield strength on increasing grain size due to amorphization occurring at grain boundaries [16]. MD simulations have also been employed to understand the dissociation of chemical bonds occurring in single-crystal CsPbI$_3$ under uniaxial and transverse loads [17]. However, this study did not focus on the mechanical response of the crystal from the perspective of stress-strain relationships and plastic deformation mechanisms [17]. Degradation mechanisms [18,19], thermal transport [20,21], ion migration [22–24], and vibrational dynamics [25,26] are other areas of interest in MHPs that have been probed using MD simulations. However, their mechanical response remains largely uninvestigated. For instance, stress-strain curves, mechanical properties such as yield, and ultimate strengths at the atomistic scale remain unknown for these materials. Furthermore, plastic deformation mechanisms in MHPs need to be investigated since they can reveal various failure modes to be mitigated or ways to intrinsically strengthen MHPs at the atomistic scale [1].

This work seeks to answer the aforementioned questions by probing the atomistic response of cesium lead iodide and bromide perovskites (CsPbI$_3$, CsPbBr$_3$, CsPbIBr$_2$, and CsPbI$_2$Br) under uniaxial compression and tension through MD simulations. In addition to determining mechanical properties and stress-strain curves at the atomistic scale, we reveal various plastic deformation mechanisms that govern the response of these materials and highlight plausible strengthening mechanisms that can lead to robust MHPs. Section II describes the development of the atomistic models and simulation procedure. Section III discusses results in two subsections that focus on the response of MHPs under uniaxial tension and compression. Section IV presents the conclusions.

II. METHODS

Since our objective was to investigate and contrast the mechanical response of all the cesium lead iodide and bromide perovskites, the fully transferrable interatomic potential (IP) proposed for this system by Balestra *et al.* [27] was utilized for the study. The functional form of the potential, which is expressed as

$$U_{ij}(r_{ij}) = A_{ij}\exp\left(-\frac{r_{ij}}{\rho_{ij}}\right) - \frac{C_{ij}}{r_{ij}^6} + \frac{1}{4\pi\varepsilon_0}\frac{q_iq_j}{r_{ij}}, \quad (1)$$

comprises Buckingham and Coulomb terms that model pairwise interactions of atoms. The parameters C_{ij} ρ_{ij}, and A_{ij} for each pair of atoms are detailed in Ref. [27]. We employed a radial cutoff of 12 Å for the repulsive exponential portion of the Buckingham term, while the $1/r_{ij}^6$ Buckingham term and the Coulombic term were utilized as full long-range potentials. Within the 12−Å cutoff, the $1/r_{ij}^6$ term and the Coulombic term are computed directly by the pair potential while beyond the cutoff, these interactions are determined
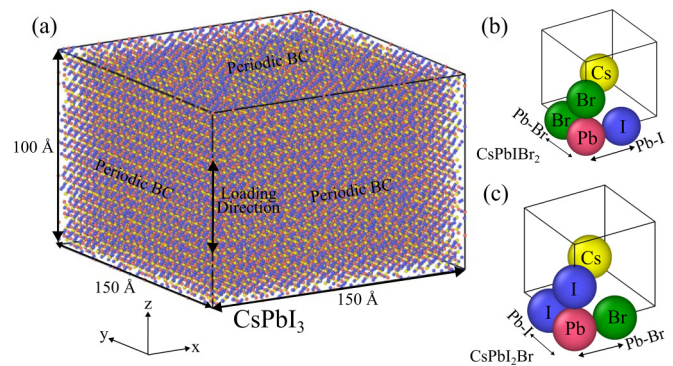

FIG. 1. (a) Representative CsPbI$_3$ domain. Direction of applied tension or compressive load aligns with z axis. Unit cells of mixed-halide perovskites (b) CsPbIBr$_2$ and (c) CsPbI$_2$Br identifying two loading directions investigated in these crystals as Pb-I and Pb-Br.

in reciprocal space. A particle-particle particle-mesh solver is utilized to determine the long-range Coulombic interactions, while a similar mesh-based long-range dispersion sum is used to calculate the $1/r_{ij}^6$ Buckingham interactions. Selecting this transferable interatomic potential [27] ensured that all the cesium lead iodide and bromide perovskites (CsPbI$_3$, CsPbBr$_3$, CsPbIBr$_2$, and CsPbI$_2$Br) could be studied using the same parameter set as opposed to using a different interatomic potential for each crystal [18,28,29]. Furthermore, no interatomic potentials currently exist for modeling the atomistic response of mixed-halide perovskites CsPbIBr$_2$, and CsPbI$_2$Br except for that proposed by Balestra *et al.* [27]. The elastic constants (Young's, bulk, and shear moduli) of these perovskites determined using this interatomic potential agree with literature while the experimentally observed interatomic distances at 300 K, variation in lattice parameters with temperature, and thermal conductivities also conform to experimental data [27]. For instance, Young's modulus of CsPbI$_3$, CsPbBr$_3$, and CsPbI$_2$Br were determined to be 22.94, 21.07, and 23.04 GPa, respectively, using this interatomic potential, while the corresponding values calculated using density-functional theory (DFT) simulations are 20.05 [30], 20.74 [31], and 18.41 [32] GPa, respectively. We have also conducted additional density-functional theory simulations to verify the applicability of this interatomic potential under large compressive and tensile strains (up to 12.5%; see Supplemental Material [33]).

MD simulations were conducted in cuboid-shaped domains of size $\sim$150$\times$150$\times$100 Å (25$\times$25$\times$17 unit cells) which comprised 53,125 atoms [see Fig. 1(a)]. The x, y, and z axes of the simulation coordinate system aligned with the [100], [010], and [001] lattice vectors, respectively, for all the perovskite single crystals analyzed in this study. The domains were first subjected to conjugate gradient energy minimization, which was followed by dynamic equilibration in the isothermal-isobaric (NPT) ensemble at 300 K and 0 atm. Next, the length of the domain along the z axis [see Fig. 1(a)] was altered at a constant strain rate of 0.0004 ps^{-1}, while the stress components along the lateral dimensions (σ_x and σ_y) were equilibrated to zero, thus resulting in a uniaxial stress state. In this manner, states of uniaxial tension or compression could be attained by lengthening or shortening, respectively,
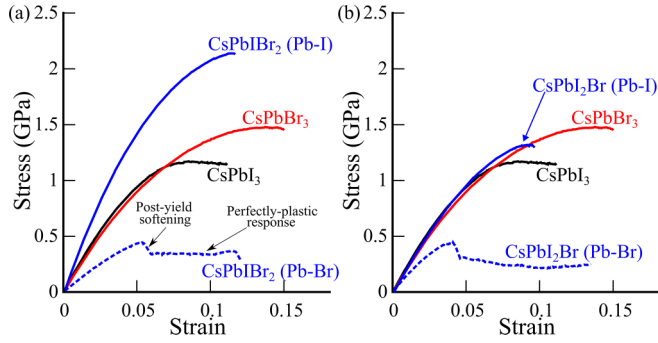
FIG. 2. Comparison of stress-strain response of mixed-halide perovskites (a) $CsPbIBr_2$ and (b) $CsPbI_2Br$ with that of $CsPbI_3$ and $CsPbBr_3$ under uniaxial tension. Two distinct loading directions in $CsPbIBr_2$ and $CsPbI_2Br$ (Pb-Br and Pb-I axes) are identified in Figs. 1(b) and 1(c).

the length of the domain along the z axis. Periodic boundary conditions were applied to all the faces of the domain, while a simulation time step of 1 fs was used. Since $CsPbI_3$ and $CsPbBr_3$ exhibit a cubic symmetry, any of their three equivalent lattice vectors can be selected for application of the uniaxial load. However, the mixed-halide perovskites $CsPbIBr_2$ and $CsPbI_2Br$ have two unique lattice vectors, which lie parallel to the Pb–I and Pb–Br bonds as shown in Figs. 1(b) and 1(c). Thus, the mechanical response was investigated along both the directions for these crystals. These loading directions will henceforth be denoted as "Pb-I" and "Pb-Br" axes. This study utilized LAMMPS [34] to conduct the molecular dynamics simulations and to generate the virtual diffraction patterns (see Ref. [35] for more details), while OVITO [36] was used for analyzing and illustrating the simulation results.

III. RESULTS AND DISCUSSION

A. Uniaxial tension

Figures 2(a) and 2(b) present the stress-strain curves under uniaxial tension for all crystals investigated in this study, while Table I summarizes Young's modulus E, yield strength σ_y, ultimate strength σ_u, and ultimate strain ε_u derived from the stress-strain curves. While Young's modulus was determined from the slope of the stress-strain curve in the range of 0.1 to 0.3 GPa, yield strength was defined as the stress that produces 0.2% plastic strain. The ultimate strength and strain were defined at the highest point on the stress-strain curve.

Our analysis finds $CsPbI_3$ and $CsPbBr_3$ to have comparable Young's modulus (22.94 and 21.07 GPa, respectively) and yield strength (0.65 and 0.62 GPa). However, $CsPbBr_3$ is found to be stronger and more ductile [see Fig. 2(a)], with higher ultimate strength and strains (1.46 GPa and 0.14, respectively) than $CsPbI_3$ (1.16 GPa and 0.08, respectively). This higher strength likely arises from the stronger metal-halide bonds in the former than the latter [1]. Both $CsPbI_3$ and $CsPbBr_3$ exhibit a smooth and monotonic increase in stress with strain until a maximum is attained (i.e., σ_u), which is followed by a stress reduction [see Fig. 2(a)]. This behavior, characterized by the absence of a clearly identifiable yield point, was also noted by Yu $et\ al.$ [16] in MD simulations of single-crystal MAPbI$_3$ subjected to uniaxial tension. Next, consider the stress-strain curves of $CsPbIBr_2$ in Fig. 2(a), obtained under the application of uniaxial tension along Pb-I and Pb-Br axes [see Fig. 1(b)]. While $CsPbIBr_2$ exhibits very high Young's modulus (32.96 GPa) and ultimate strength (2.13 GPa) along the Pb-I axis, a very compliant response ($E = 9.24$ GPa) with low yield strength (0.43 GPa) was noted on loading along the Pb-Br axis. Stress-strain curves obtained along the Pb-I and Pb-Br axes in $CsPbI_2Br$ also exhibited similar traits [see Fig. 2(b)], with the elastic modulus and ultimate strength along the Pb-I axis (23.04 and 1.298 GPa, respectively) being higher than along the Pb-Br axis (13.05 and 0.424 GPa, respectively). The anisotropic response of mixed-halide perovskites also extends to their postyield behavior. Along the Pb-I axis in $CsPbIBr_2$, a smooth transition from linear to nonlinear regime is observed, like that seen in $CsPbI_3$ and $CsPbBr_3$. In contrast, the stress-strain curve along the Pb-Br axis exhibits a distinct yield point which is followed by a postyield softening response and perfectly plastic behavior [see Fig. 2(a)]. A similar postyield response is also noted along the Pb-Br axis in $CsPbI_2Br$ [Fig. 2(b)], hinting at the presence of the same plastic deformation mechanism in both the mixed-halide perovskites when loaded along the Pb-Br axis.

Figure 3(a) presents contour plots of atomic strain along the direction of tension (i.e., ε_{zz}) in $CsPbI_3$ at three instants P1, P2, and P3 on the stress-strain curve [see Fig. 3(c)]. $CsPbI_3$ exhibits a homogeneous deformation behavior under uniaxial tension, which is characterized by uniform distribution of strains in the domain without any localization [see snapshots at P1, P2, and P3 in Fig. 3(a)]. We noted a similar behavior (i.e., homogeneity in atomic-strain distribution throughout the loading duration) under tension also in $CsPbBr_3$, and the mixed-halide perovskites ($CsPbIBr_2$ and $CsPbI_2Br$) when

TABLE I. Mechanical properties of MHPs obtained from MD simulations under uniaxial tension and compression.

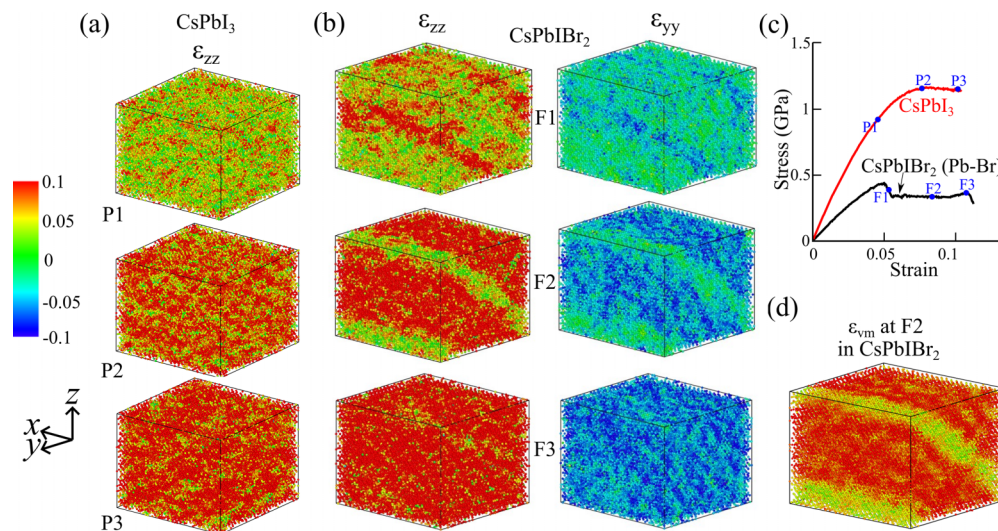| Perovskite (Loading direction)	E (GPa)	Tension (GPa)			Compression (GPa)		
		σ_y	σ_u	ε_u	σ_y	σ_u	ε_u
$CsPbI_3$	22.941	0.646	1.157	0.084	1.520	2.234	0.147
$CsPbBr_3$	21.072	0.617	1.463	0.143	3.220	3.311	0.110
$CsPbIBr_2$ (Pb-I)	32.958	1.134	2.133	0.115	3.957	3.957	0.074
$CsPbIBr_2$ (Pb-Br)	9.235	0.430	0.430	0.052	0.701	0.701	0.054
$CsPbI_2Br$ (Pb-I)	23.042	0.588	1.298	0.095	1.139	1.139	0.041
$CsPbI_2Br$ (Pb-Br)	13.050	0.408	0.424	0.040	1.276	1.276	0.069

FIG. 3. Contour plots of atomic strain components in (a) CsPbI$_3$, and (b) CsPbIBr$_2$ when loaded in tension along Pb-Br axis [see Fig. 1(b)]. (c) Stress-strain response of CsPbI$_3$ and CsPbIBr$_2$, with frames shown in (a) and (b) annotated on curve. (d) Contour plot of atomic von Mises shear strain (ε_{vm}) in CsPbIBr$_2$ at instant F2 depicted in (b).

loaded along the Pb-I axis. Furthermore, such a homogeneous response was also noted by Yu *et al.* [16] in MD simulations of uniaxial tension in single-crystal cubic MAPbI$_3$. In contrast, consider Fig. 3(b), which depicts the distribution of atomic strain along the direction of tension (ε_{zz}) and a lateral direction (ε_{yy}) in CsPbIBr$_2$ when loaded along the Pb-Br axis. Strain components are depicted at three instants on the stress-strain curve (F1, F2, and F3) as identified in Fig. 3(c). While the distribution of atomic strains was homogeneous until the yield point, the onset of postyield softening [see F1 in Fig. 3(c)] was noted to be accompanied by the occurrence of very high axial strain ε_{zz} in certain localized regions of the domain [see red-colored regions in frame F1 in Fig. 3(b)]. These localized regions also experienced high lateral strains ε_{yy} (see dark-blue colored regions in frame F1), which is indicative of lateral contraction akin to necking. Thus, there is a localized loss of load-bearing capacity in these regions. As the domain progresses through the perfectly plastic region [F1 to F3 in Fig. 3(c)], these highly strained regions assume the form of bands that increase in thickness. Once the bands engulf the whole domain, no additional load can be sustained and structural instability sets in, as observed in the drop in stress beyond F3. Figure 3(d), which presents a contour plot of von Mises shear strain at F2, reveals these regions to be bands of high von Mises shear strain. Thus, it is the formation and growth of these bands that underlies the perfectly plastic response of CsPbIBr$_2$. We noted this mechanism to also underlie the perfectly plastic response exhibited by CsPbI$_2$Br when loaded along the Pb-Br axis [see Fig. 2(b)]. Thus, a homogeneous deformation mode is favored under uniaxial tension in CsPbI$_3$, CsPbBr$_3$, and the mixed-halide perovskites (CsPbIBr$_2$ and CsPbI$_2$Br) when loaded along the Pb-I axis, while formation and growth of bands of high von Mises shear strain dominate plastic deformation in mixed-halide perovskites when loaded along the Pb-Br axis. A similar plastic deformation mechanism, characterized by formation and growth of bands of high directional shear strain or von Mises shear strain, has also been observed in bulk

metallic glasses (BMGs) [37–39]. Thus, approaches aimed at improving mechanical response of BMGs, such as introducing interfaces and secondary phases to hinder the growth of shear bands [39], may be useful to impede the growth of bands seen in Fig. 3(b). Interestingly, traits that are characteristic of other material classes like amorphous/glassy ceramics and polymers, such as crack-tip blunting and nanovoid formation, were also noted by Yu *et al.* [16] in their MD simulations of uniaxial tension in single-crystal MAPbI$_3$. The authors further noted that dislocations play a minor role in the plastic deformation of MAPbI$_3$, with nanovoid formation, coalescence, and growth inferred to be the primary plastic deformation mechanism [16]. In the next section, we present the mechanical response of cesium lead iodide and bromide perovskites to uniaxial compression.

B. Uniaxial compression

Figure 4(a) presents the stress-strain curves for CsPbI$_3$ and CsPbBr$_3$ when subjected to uniaxial compression, while
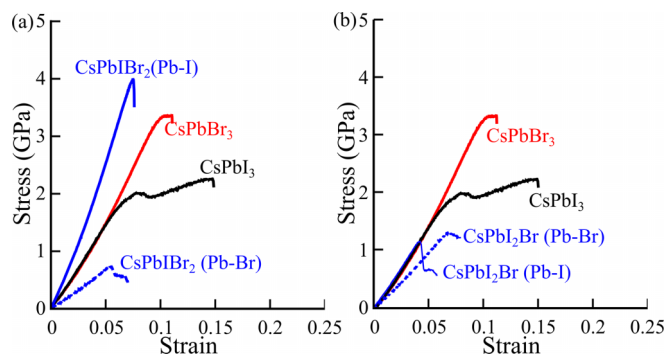

FIG. 4. Comparison of stress-strain response of mixed-halide perovskites (a) CsPbIBr$_2$ and (b) CsPbI$_2$Br with those of CsPbI$_3$ and CsPbBr$_3$ under uniaxial compression. Two distinct loading directions investigated in CsPbIBr$_2$ and CsPbI$_2$Br (Pb-Br and Pb-I axes) are identified in Figs. 1(b) and 1(c).

Table I summarizes the yield strength σ_y, ultimate strength σ_u, and ultimate strain ε_u derived from the stress-strain curves. By contrasting the stress-strain response of these crystals under tension [Fig. 2(a)] and compression, we highlight the following points. Both CsPbI$_3$ and CsPbBr$_3$ exhibit a distinct linear and nonlinear regime under uniaxial compression [see Fig. 4(a)], as opposed to the smooth transition between the regimes noted under uniaxial tension [see Fig. 2(a)]. Further, as previously observed under tension, CsPbBr$_3$ exhibits higher yield and ultimate strength (3.22 and 3.31 GPa, respectively) than CsPbI$_3$ (1.52 and 2.23 GPa, respectively) under compression. Even so, it is interesting to note that CsPbI$_3$ exhibits a much higher ultimate strain ($\varepsilon_u = 0.147$) than CsPbBr$_3$ ($\varepsilon_u = 0.110$) under compression, while the opposite was true under tension [see Fig. 2(a)]. Thus, while CsPbBr$_3$ is stronger than CsPbI$_3$ under uniaxial compression, the latter is more ductile. In fact, we noted that CsPbI$_3$ exhibits the highest ultimate strain under uniaxial compression out of all the crystals analyzed in this study (see Table I). This extended plastic regime is likely due to CsPbI$_3$ being the only crystal that exhibits postyield hardening under uniaxial compression. While the stress-strain curve for CsPbBr$_3$ flattens out beyond the elastic regime with very low postyield strain accumulation [see Fig. 4(a)], CsPbI$_3$ exhibits a drop in stress that is followed by subsequent hardening until the ultimate strength is attained. The mechanism of plastic deformation underlying this hardening phenomenon will be discussed going forward. Figures 4(a) and 4(b) also compare the stress-strain response of the mixed-halide perovskites to that of CsPbI$_3$ and CsPbBr$_3$. Recall that under uniaxial tension, a smooth transition from the linear to the nonlinear regime was noted along the Pb-I axis in CsPbIBr$_2$ and CsPbI$_2$Br [see Figs. 2(a) and 2(b)]. However, under uniaxial compression, the stress-strain curves along both the axes (i.e., Pb-I and Pb-Br) in the two crystals exhibit a distinct yield point that is followed by an abrupt drop in stress. Thus, under uniaxial compression, we do not observe the extended perfectly plastic response that was noted along the Pb-Br axis in CsPbIBr$_2$ and CsPbI$_2$Br under tension [see Figs. 2(a) and 2(b)]. A possible reason for this substantial difference in stress-strain behavior under tension and compression will be presented later.

Figure 5(a) presents contour plots of von Mises shear strain in CsPbBr$_3$ when subjected to uniaxial compression, at three instants F1, F2, and F3 marked on the stress-strain curve in Fig. 5(c). We noted CsPbBr$_3$ to exhibit homogeneous deformation under uniaxial compression, which is characterized by a mostly uniform strain distribution from the elastic regime [F1 in Fig. 5(a)], through the yield point (F2) until the end of the plastic regime (F3). While CsPbI$_3$ also exhibited a similar homogeneous response in the elastic regime, the postyield behavior of CsPbI$_3$ differed substantially from that of CsPbBr$_3$. Consider Fig. 5(c), which identifies three instants P1, P2, and P3 on the stress-strain curve of CsPbI$_3$ subjected to uniaxial compression. Figure 5(b) depicts the distribution of atomic shear strain γ_{xy} on a plane normal to the direction of compression at these instants, with atoms having positive and negative γ_{xy} colored red and blue, respectively. At P1, which lies within the elastic regime, the distribution of γ_{xy} does not assume any particular pattern thus indicating that the deformation of the crystal is homogeneous. However, once the
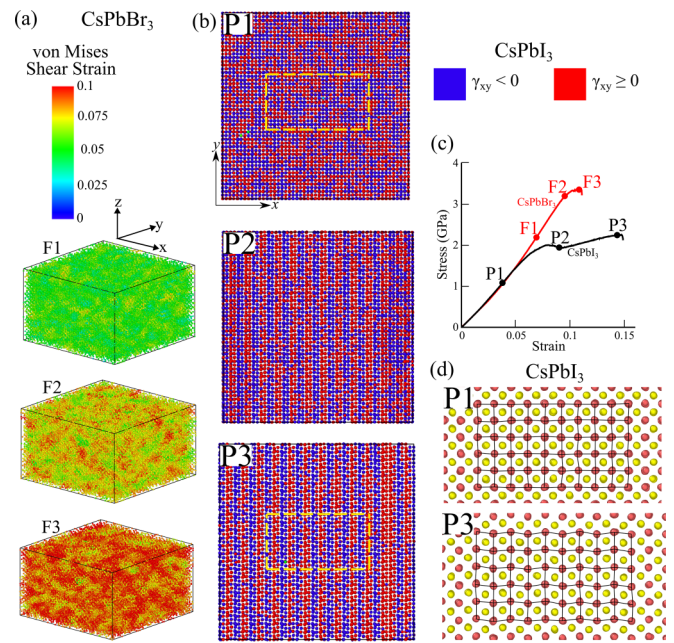

FIG. 5. (a) Contour plots of von Mises shear strain at three instants on stress-strain curve of CsPbBr$_3$ when subjected to uniaxial compression. (b) Distribution of atomic shear strain γ_{xy} (as viewed along loading direction (z axis)) at three instants on stress-strain curve of CsPbI$_3$ under uniaxial compression. Atoms with $\gamma_{xy} \geqslant 0$ and $\gamma_{xy} < 0$ are colored red and blue, respectively. (c) Stress-strain curves of CsPbI$_3$ and CsPbBr$_3$ depicting instants visualized in (a) and (b). (d) Magnified subset of area in panel (b) that is identified by dashed yellow lines at instants P1 and P3. Cesium and lead atoms are colored yellow and pink, respectively, while iodine atoms are hidden for clarity.

crystal yields [at P2 in Fig. 5(b)], the shear-strain distribution assumes a form of alternating bands of positive (red) and negative (blue) values. This strain distribution intensifies as the crystal accumulates more plastic strain [see P3 in Fig. 5(b)]. The average absolute value of γ_{xy} in both the red and blue regions was determined to be 4.2%. To explain the origins of this shear-strain distribution, Fig. 5(d) presents magnified atomic snapshots of the regions circumscribed by yellow lines at instants P1 and P3 in Fig. 5(b). In these snapshots, lead and cesium atoms are colored pink and yellow, respectively, while iodine atoms have been hidden to enable clear identification of the cubic unit cells comprising the domain. At P1 in Fig. 5(d), the deformation of the domain is homogeneous and elastic, with negligible distortion of the cubic unit cells. However, by P3 (which lies near the end of the plastic regime), we note that every alternate column of unit cells exhibits similar deformation, while adjacent columns of unit cells are symmetrically distorted. It is this distortion of the unit cells that results in the strain field observed at P3 in Fig. 5(b). We were interested in understanding the atomistic mechanisms that underlie these phenomena. Thus, we evaluated MD-derived fast Fourier transform (FFT) optical diffractograms of the CsPbI$_3$ domain to probe for potential evolution of defects under uniaxial compression. Figures 6(a)–6(c) present the diffractograms at the unstrained state, and states P2, and P3 identified in Fig. 5(c). These diffractograms were obtained along the [001] zone axis
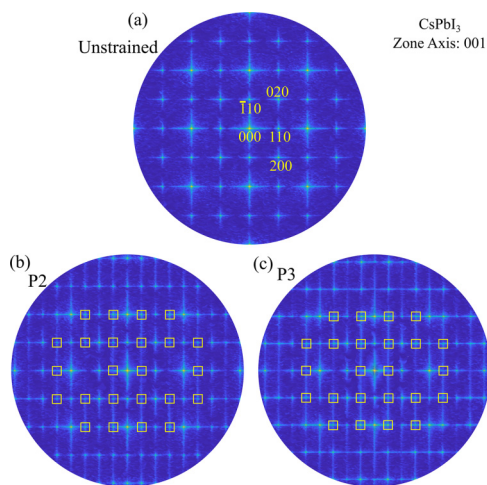
FIG. 6. Optical diffraction patterns derived from FFT of MD simulations ([001] zone axis) of single-crystal $CsPbI_3$ when subjected to uniaxial compression along [001] at (a) unstrained state, (b) P2, and (c) P3 depicted in Fig. 5(c).
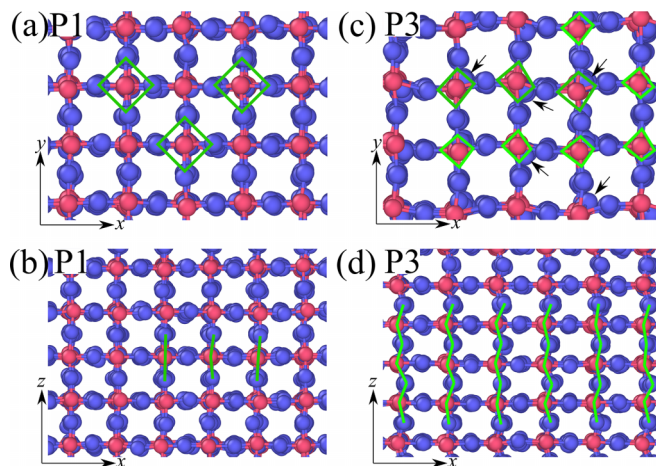

FIG. 7. The Pb-I coordination environment in $CsPbI_3$ at instants P1 [panels (a) and (b)] and P3 [panels (c) and (d)] identified on the stress-strain curve in Fig. 5(c). While panels (a) and (c) depict the view along the axis of compression (z axis), panels (b) and (d) present view along lateral direction (y axis). Iodine and lead atoms are colored blue and pink, respectively, while cesium atoms are hidden.

(also the axis of compression) and are indexed as shown in Fig. 6(a). We noted that onset of plastic deformation marks the emergence of new reflections in the diffraction pattern as shown in Fig. 6(b) (see yellow squares). These new reflections are periodic and occur at half the period of the original ones. Further, they persist under increasing plastic strain, as seen at P3 in Fig. 6(c). In prior investigations on perovskites, such reflections have been attributed to periodic arrays of crystal defects. For instance, Chen *et al.* [40] noted that point defects such as spatially periodic arrays of MA^+ vacancies in $MAPbI_3$ produce superlattice spots in the FFT patterns of high-resolution transmission electron microscope images. Such superlattice reflections can also arise from changes to the $B-X$ coordination environment (in ABX_3 perovskites) such as in-phase or antiphase tilting of the $B-X$ octahedra due to deviations from cubic symmetry [41]. Interestingly, our work also finds the onset of these superlattice reflections to be related to deformation-induced changes to the $B-X$ octahedra. Consider Fig. 7(a), which presents a magnified view of the domain along the axis of compression (z axis) at P1. Lead and iodine atoms are colored pink and blue, respectively, while cesium atoms are hidden. At P1, the 6 iodine atoms are symmetrically distributed around each lead atom, with 4 atoms lying in the x-y plane [see Fig. 7(a)] and 2 atoms lying above and below each lead atom along the z axis [see Fig. 7(b)]. However, at P3 [Fig. 7(c)], the Pb-I coordination is distorted, with some iodine atoms (marked by black arrows) visibly displaced from their ideal location beneath the lead atom. As a result, the Pb-I octahedra are systematically distorted due to the change in the I–Pb–I bond angle from 180° [see Fig. 7(d)]. It is these defects, in the form of distorted octahedra, that underlie the superlattice reflections noted at P2 and P3 in Figs. 6(b) and 6(c). Furthermore, since these reflections form right after yielding [at P2 in Fig. 6(b)], they also possibly underlie the postyield hardening observed in the stress-strain curve of $CsPbI_3$. The higher ultimate strain exhibited by $CsPbI_3$ under uniaxial compression ($\varepsilon_u = 0.147$ in Table I) compared to all other crystals is also a likely outcome

of this defect-induced strengthening. This study thus provides evidence of defect generation in cesium lead halides under mechanical loading and indicates the potential for strengthening MHP films by engineering defects into the material [1].

Next, we discuss plastic deformation mechanisms occurring in $CsPbIBr_2$ and $CsPbI_2Br$ under uniaxial compression. $CsPbIBr_2$, when compressed along the Pb-I axis, exhibited homogeneous deformation until the elastic limit that was characterized by a uniform distribution of strains in the domain (see Fig. S2 in Supplemental Material [33]). Localized regions of high strains emerged beyond the elastic limit, which indicated the onset of structural instability and cohered with the abrupt drop in stress noted on the stress-strain curve [see Fig. 4(a)]. Thus, $CsPbIBr_2$ exhibited negligible plastic deformation when compressed uniaxially along the Pb-I axis. In contrast, consider Fig. 8(a), which identifies two instants on the stress-strain curve of $CsPbIBr_2$ when compressed along the Pb-Br axis, while Fig. 8(b) presents atomic snapshots at these instants. While a homogeneous deformation is observed until the elastic limit [see F1 in Fig. 8(b)], bands of high von Mises shear strain develop beyond the yield point [see F2 in Fig. 8(b)]. A very similar response is also exhibited by $CsPbI_2Br$ when uniaxially compressed along the Pb-Br axis [see P1 and P2 in Fig. 8(c)]. Thus, bands of high shear strain form in the mixed-halide perovskites under both uniaxial tension and compression along the Pb-Br axis. Recall that under tension, formation and growth of these bands was accompanied by a perfectly plastic response [see Fig. 3(c)]. In contrast, we note a continuous postyield reduction in stress under compression [see Fig. 8(a)]. This absence of a perfectly plastic response under uniaxial compression likely stems from differences in the failure modes of brittle materials under uniaxial tension and compression. While fracture normal to the loading direction occurs in brittle materials under uniaxial tension, failure via longitudinal splitting cracks is favored under uniaxial compression [42]. Thus, formation of these bands
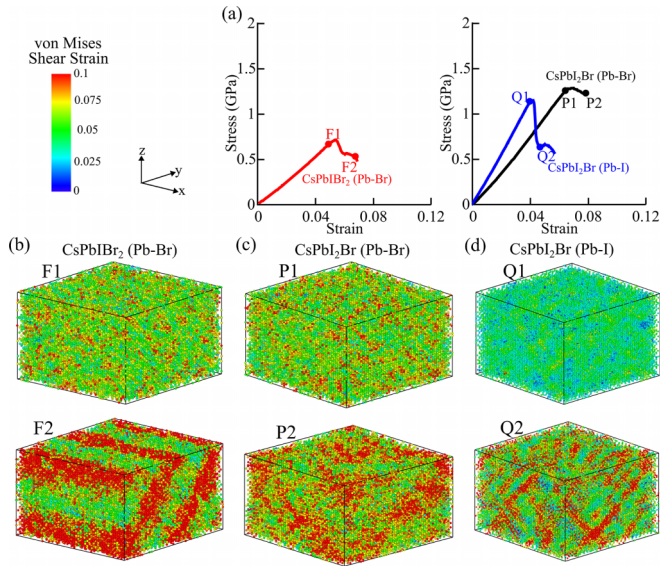
FIG. 8. (a) Stress-strain curves of CsPbIBr$_2$ and CsPbI$_2$Br when subjected to uniaxial compression, with two instants identified on curves. Contour plots of atomic von Mises shear strain (ε_{vm}) at two instants in (b) CsPbIBr$_2$ when compressed along Pb-Br axis, and CsPbI$_2$Br when compressed along (c) Pb-Br and (d) Pb-I axes.

of locally weakened material across the loading direction [i.e., z dimension of the domain, as seen at F2 and P2 in Figs. 8(b) and 8(c), respectively] is enough to induce structural instability under uniaxial compression. However, under tension, the material can still be loaded until the band gradually grows and engulfs the domain [see F1, F2, and F3 in Fig. 3(b)], thus resulting in the extended perfectly plastic response observed in Fig. 3(c). Finally, consider Fig. 8(d), which presents atomic snapshots at instants Q1 and Q2 on the stress-strain curve of CsPbI$_2$Br, when subjected to uniaxial compression along the Pb-I axis. Even here, we note a postyield reduction in stress, arising from the growth of bands of high shear strain. Note that the drop in stress for this case [Q1 to Q2 in Fig. 8(a)] is more drastic than that in the other stress-strain curves in Fig. 8(a). The highly delocalized formation of multiple bands [at Q2 in Fig. 8(d)] likely underlies this more dramatic drop in strength, while at F2 and P2 [Figs. 8(b) and 8(c), respectively], growth of one or two major bands dominates the plastic response. Thus, formation and growth of bands of high von Mises strain dominates the plastic response of CsPbIBr$_2$ along the Pb-Br axis, and CsPbI$_2$Br along the Pb-I and Pb-Br axes.

This study thus systematically analyzed the formation and evolution of defects as single-crystal cesium lead iodide and bromide perovskites are plastically deformed under uniaxial tension and compression. In addition to identifying mechanisms that strengthen and weaken MHPs under mechanical deformation, these simulations provide insights into plausible mechanisms that operate under experimental conditions. For instance, the defect-induced strengthening revealed here

might underlie the strain hardening noted under nanoindentation in MHPs, in addition to dislocation slip that has been suggested [14,15]. More importantly, our study shows the potential for strengthening MHPs through tuning of defect microstructure (such as engineering dislocations, twins, and grain-size distribution), which is an approach well studied in other materials.

IV. CONCLUSION

This study investigated the mechanical response of single-crystal cesium lead iodide and bromide perovskites (CsPbI$_3$, CsPbBr$_3$, CsPbIBr$_2$, and CsPbI$_2$Br) under uniaxial tension and compression using MD simulations. While CsPbI$_3$ and CsPbBr$_3$ exhibited a homogeneous response and a smooth elastic to plastic transition under uniaxial tension, CsPbIBr$_2$ and CsPbI$_2$Br exhibited considerable anisotropy in plastic behavior. A smooth elastic to plastic transition, similar to that exhibited by CsPbI$_3$ and CsPbBr$_3$, was noted along the lead-iodine axis in the mixed-halide perovskites under uniaxial tension. However, a distinct yield point followed by a perfectly plastic response was noted along the lead-bromine axis. Formation and growth of bands of high von Mises shear strain is identified as the mechanism underlying this perfectly plastic response. CsPbBr$_3$ is found to be both stronger (higher yield and ultimate strength) and more ductile than CsPbI$_3$ under uniaxial tension, while the latter is more ductile under uniaxial compression. While CsPbBr$_3$ exhibits negligible plastic deformation under uniaxial compression, CsPbI$_3$ accumulates considerable plastic strain that is accompanied by a hardening response. CsPbIBr$_2$ is shown to exhibit negligible plastic deformation when uniaxially compressed along the lead-iodine axis, while formation and growth of bands of high von Mises shear strain occurs on compressing along the lead-bromine axis. Formation of these bands also characterizes the plastic response of CsPbI$_2$Br along both lead-iodine and lead-bromine axes under uniaxial compression. CsPbI$_3$ is noted to be the only perovskite in this study that exhibits strain hardening under uniaxial compression, which is attributed to the generation of defects in the plastic regime. These defects, which take the form of deformation-induced distortion of the Pb-I octahedra, manifest as superlattice reflections in optical diffraction patterns derived from FFT analysis of MD simulations. This study thus demonstrates the possibility of intrinsically strengthening MHPs through tailoring of defect microstructure, while providing insights into plausible mechanisms that operate in these materials under experimental conditions of mechanical deformation.

[1] Q. Tu, D. Kim, M. Shyikh, and M. G. Kanatzidis, Matter **4**, 2765 (2021).

[2] Y. Liu, P. A. Chen, and Y. Y. Hu, J. Mater. Chem. C **8**, 16691 (2020).

[3] K. Y. Ji, M. Anaya, A. Abfalterer, and S. D. Stranks, Adv. Opt. Mater. **9**, 2002128 (2021).

[4] H. Y. Dong, C. H. Zhang, X. L. Liu, J. N. Yao, and Y. S. Zhao, Chem. Soc. Rev. **49**, 951 (2020).

[5] X. Hu, X. D. Zhang, L. Liang, J. Bao, S. Li, W. L. Yang, and Y. Xie, Adv. Funct. Mater. **24**, 7373 (2014).

[6] C. C. Stoumpos and M. G. Kanatzidis, Adv. Mater. **28**, 5778 (2016).

[7] K. Frohna and S. D. Stranks, in *Handbook of Organic Materials for Electronic and Photonic Devices*, 2nd ed., edited by O. Ostroverkhova (Woodhead Publishing, Cambridge, England, 2019), p. 211.

[8] M. C. Brennan, S. Draguta, P. V. Kamat, and M. Kuno, ACS Energy Lett. **3**, 204 (2018).

[9] L. Chouhan, S. Ghimire, C. Subrahmanyam, T. Miyasaka, and V. Biju, Chem. Soc. Rev. **49**, 2869 (2020).

[10] D. B. Kim, J. W. Lee, and Y. S. Cho, Adv. Funct. Mater. **31**, 2007131 (2021).

[11] S. Y. Lee, S. H. Kim, Y. S. Nam, J. C. Yu, S. Lee, D. B. Kim, E. D. Jung, J. H. Woo, S. Ahn, S. Lee *et al.*, Nano Lett. **19**, 971 (2019).

[12] Z. H. Dai, M. C. Doyle, X. Liu, M. Hu, Q. Wang, C. E. Athanasiou, Y. Liu, B. W. Sheldon, H. Gao, S. Liu *et al.*, Scr. Mater. **223**, 115064 (2023).

[13] M. Park, H. J. Kim, I. Jeong, J. Lee, H. Lee, H. J. Son, D. E. Kim, and M. J. Ko, Adv. Energy Mater. **5**, 1501406 (2015).

[14] M. A. Reyes-Martinez, A. L. Abdelhady, M. I. Saidaminov, D. Y. Chung, O. M. Bakr, M. G. Kanatzidis, W. O. Soboyejo, and Y. L. Loo, Adv. Mater. **29**, 1606556 (2017).

[15] L. Ma, W. Li, K. Yang, J. Bi, J. Feng, J. Zhang, Z. Yan, X. Zhou, C. Liu, Y. Ji *et al.*, APL Mater. **9**, 041112 (2021).

[16] J. G. Yu, M. C. Wang, and S. C. Lin, ACS Nano **10**, 11044 (2016).

[17] S. Kumar, T. Mishra, and R. K. Sahu, J. Mater. Chem. C **10**, 12091 (2022).

[18] M. Pols, J. M. Vicent-Luna, I. Filot, A. C. T. van Duin, and S. X. Tao, J. Phys. Chem. Lett. **12**, 5519 (2021).

[19] M. Pols, T. Hilpert, I. A. W. Filot, A. C. T. van Duin, S. Calero, and S. X. Tao, ACS Appl. Mater. Interfaces **14**, 40841 (2022).

[20] A. Mattoni, A. Filippetti, and C. Caddeo, J. Phys.: Condens. Matter **29**, 043001 (2017).

[21] Y. F. Gao, W. B. Ning, X. L. Zhang, Y. Z. Liu, Y. G. Zhou, and D. W. Tang, Nano Energy **82**, 105747 (2021).

[22] P. Delugas, C. Caddeo, A. Filippetti, and A. Mattoni, J. Phys. Chem. Lett. **7**, 2356 (2016).

[23] D. Barboni and R. A. De Souza, Energy Environ. Sci. **11**, 3266 (2018).

[24] D. Kemp and R. A. De Souza, Phys. Rev. Mater **5**, 105401 (2021).

[25] A. Mattoni, A. Filippetti, M. I. Saba, and P. Delugas, J. Phys. Chem. C **119**, 17421 (2015).

[26] A. Mattoni, A. Filippetti, M. I. Saba, C. Caddeo, and P. Delugas, J. Phys. Chem. Lett. **7**, 529 (2016).

[27] S. R. G. Balestra, J. M. Vicent-Luna, S. Calero, S. X. Tao, and J. A. Anta, J. Mater. Chem. A **8**, 11824 (2020).

[28] S. S. I. Almishal and O. Rashwan, RSC Adv. **10**, 44503 (2020).

[29] R. Pascazio, F. Zaccaria, B. van Beek, and I. Infante, J. Phys. Chem. C **126**, 9898 (2022).

[30] S. Li, S. G. Zhao, H. Q. Chu, Y. Gao, P. Lv, V. Wang, G. Tang, and J. W. Hong, J. Phys. Chem. C **126**, 4715 (2022).

[31] M. Roknuzzaman, K. Ostrikov, H. X. Wang, A. J. Du, and T. Tesfamichael, Sci. Rep. **7**, 14025 (2017).

[32] P. M. Maleka, R. S. Dima, O. M. Ntwaeaborwa, and R. R. Maphanga, Mater. Today: Proc. **62**, S12 (2022).

[33] See Supplemental Material at http://link.aps.org/supplemental/10.1103/PhysRevMaterials.7.083604 for (a) details of DFT simulations conducted to check the applicability of the interatomic potential under high compressive and tensile strains, and (b) mechanical response of $CsPbIBr_2$ subjected to uniaxial compression along the Pb-I axis.

[34] S. Plimpton, J. Comput. Phys. **117**, 1 (1995).

[35] S. P. Coleman, D. E. Spearot, and L. Capolungo, Modell. Simul. Mater. Sci. Eng. **21**, 055020 (2013).

[36] A. Stukowski, Modell. Simul. Mater. Sci. Eng. **18**, 015012 (2010).

[37] D. Sopu, Y. Ritter, H. Gleiter, and K. Albe, Phys. Rev. B **83**, 100202(R) (2011).

[38] Q. K. Li and M. Li, Appl. Phys. Lett. **91**, 231905 (2007).

[39] K. Albe, Y. Ritter, and D. Sopu, Mech. Mater. **67**, 94 (2013).

[40] S. Chen, C. Wu, Q. Shang, Z. Liu, C. He, W. Zhou, J. Zhao, J. Zhang, J. Qi, Q. Zhang *et al.*, Acta Mater. **234**, 118010 (2022).

[41] D. I. Woodward and I. M. Reaney, Acta Cryst. B **61**, 387 (2005).

[42] Y. A. Fishman, Int. J. Rock Mech. Miner. Sci. **45**, 993 (2008).